The Hybrid Drive: a chronic implant device combining tetrode arrays with silicon probes for layer-resolved ensemble electrophysiology in freely moving mice

Matteo Guardamagna[1,†], Ronny Eichler[1], Rafael Pedrosa[1], Arno Aarts[3], Arne F. Meyer[1,2,*] and Francesco P. Battaglia[1,*]

[1]Donders Institute for Brain, Cognition and Behaviour, Radboud University, Nijmegen, the Netherlands

[2]Sainsbury Wellcome Centre for Neural Circuits and Behaviour, University College London, London, UK

[3]ATLAS Neuroengineering, Leuven, Belgium

[*] Co-senior author

[†]Correspondence: (matteo.guardamagna@donders.ru.nl)

Summary

Understanding the function of brain cortices requires simultaneous investigation at multiple spatial and temporal scales and to link neural activity to an animal's behavior. A major challenge is to measure within- and across-layer information in actively behaving animals, in particular in mice that have become a major species in neuroscience due to an extensive genetic toolkit. Here we describe the Hybrid Drive, a new chronic implant for mice that combines tetrode arrays to record within-layer information with silicon probes to simultaneously measure across-layer information. The flexible, open-source design allows custom spatial arrangements of tetrode arrays and silicon probes to generate areas-specific layouts. We show that large numbers of neurons and layer-resolved local field potentials can be recorded from the same brain region across weeks without loss in electrophysiological signal quality. The drive's light-weight structure (≈ 3.5 g) leaves animal behavior largely unchanged during a variety of experimental paradigms, enabling the study of rich, naturalistic behaviors. We demonstrate the power of the Hybrid Drive in a series of experiments linking the spiking activity of CA1 pyramidal layer neurons to the oscillatory activity across hippocampal layers.

Introduction

A major goal in neuroscience is to understand the function of the nervous system at a variety of levels, from single cells to entire networks that mediate complex behaviors such as navigation, foraging, and social interaction in natural settings. The mouse has emerged as an important species in neuroscience due to the availability of genetic tools that can reveal the precise mechanisms at the circuit level and link these to the animal's behavior (Luo et al., 2008). In particular, many brain structures (including the cortex and the hippocampus) are organized in layers with information processing within and also across the layers (Andersen et al., 1971, Amaral and Witter, 1989, Andersen et al., 2006). Simultaneously measuring neural activity at these two dimensions while an animal is interacting with its environment remains a major challenge, especially in the mouse with its relatively small size (body weight of an adult male mouse ≈ 25 grams). To address this challenge, we developed a chronic implant to measure neural activity within and across layers in freely moving mice.

Tetrodes are a standard method for neuronal recordings in behaving animals, in particular for chronic recordings of many neurons for extended time periods in freely moving rodents (McNaughton et al., 1983, Wilson and McNaughton, 1993, Gothard et al., 1996). The precision, stability and bio-compatibility of tetrode implants enable recordings for months from the same local circuit (Voigts et al., 2013, 2020). Modern tetrode implants enable highly flexible arrangements of tetrodes that can easily be modified depending on the set of target areas. By performing small and repeated adjustments of individual tetrodes, it is possible to maximize cell yield and to target specific layers (Harris et al., 2000) or structures deep in the brain (Chen et al., 2020) without the need to remove overlying structures as for optical imaging

methods. However, a disadvantage of tetrodes is that they do not easily allow for measuring the activity across layers with a well-defined geometrical arrangement of recording sites.

High-density silicon probes (Buzsaki et al., 2015), on the other end, offer unparalleled opportunities for populations recordings across several layers or even from multiple brain regions in head-fixed (Steinmetz et al., 2019) or freely moving animals (Steinmetz et al., 2021). Their geometric design – electrodes are typically arranged along one or more shafts – enables superior anatomical localization, given the well-defined distances between recording sites. Yet, silicon probes lack the flexibility of tetrodes arrays which can easily be arranged in different geometric layouts to sample different locations along a single layer. While custom silicon probe designs are possible, they are typically expensive and tailored to a single brain structure. Ideally, one would combine in a single device the flexibility of tetrode arrays, to record neural activity within layers, and silicon probes to record activity across layers.

Here we describe the Hybrid Drive, a novel chronic implant that combines the advantages of tetrodes and flexible-shaft silicon probes in a single, lightweight device. A core feature of the Hybrid Drive is its flexible design; the spatial arrangement of tetrodes and silicon probes can be modified depending on the set of target areas and their depths can individually be adjusted even after implantation. Similarly, the choice of the silicon probe type can be adapted to match the three-dimensional organization of the desired brain areas (e.g., the tonotopic organization of sensory cortices). Importantly, the overall weight of the implant ($\approx$ 3.5 grams) enables studies in freely moving animals, including mice.

We show that the ability of the Hybrid Drive to record single cells with tetrodes is not affected by the presence of a silicon probe (and vice versa) and patterns of behavior are largely unchanged by the drive implant. We further demonstrate the potential of the Hybrid Drive in a series of experiments in freely moving mice, focusing on recordings from the hippocampal CA1 region. First, we show that the interactions of single cells and layer-specific local field potentials in CA1 strongly vary with the animal's behavior, across slow and fast time scales. Second, we show that single cells in the hippocampal pyramidal layer integrate across-layer information, in addition to spatial variables typically studied in navigation experiments. This integration is layer-specific, is consistent across different animals, and improves the prediction accuracy of the cells' responses. These results already demonstrate that the Hybrid Drive can lead to novel insights into the interactions between neural processes occurring within and across layers and the animal's behavior.

Results

A chronic implant for simultaneous measurements of within-layer and across-layer neural activity in freely moving mice.

The Hybrid Drive consists of a custom chronically implantable tetrode drive (based on an existing implant design; Voigts et al. (2013)) which can include up to two silicon probes (Figure 1A). The 14 independently movable tetrodes enable flexible recordings of local activity, e.g., from neurons within the same cortical or hippocampal layer; the two movable silicon probes provide across-layer information. The weight of the whole assembly is $\approx$ 3.5 g. This enables the study of naturalistic behaviors, such as navigation, exploration, and social interactions in unrestrained animals.

A key feature of the implant is the flexible design of the guide array holding the tetrodes and silicon probes (Figure 1A). For example, the position and angle of the silicon probes relative to the tetrodes or the angle of the overall assembly can easily be modified depending on brain areas under investigation or scientific question. In the current design, we used one or two 16-channel probes (E16R_60_S1_L20_NT with 60 µm pitch between contacts, ATLAS Neuroengineering, Belgium) with a custom electrode interface board (EIB; Figures S3B–D; Figure S3). This design was optimized for long-term recordings in the hippocampus, a brain region that is widely being studied in freely moving rodents; the use of Omnetics connectors on the EIB ensures compatibility with most modern neural recording systems, including the Open Ephys acquisition system (Siegle et al., 2017). However, the design of the EIB and guide tube array can be adapted to incorporate the latest silicon probes, as long as the shaft can withstand a bending angle of approximately 25°. Silicon probe shaft flexibility is another key feature of the Hybrid Drive's design (Herwik et al., 2011); it facilitates insertion of the probe in the guide tubing during drive building (Figure S2) and provides additional protection from mechanical shocks, e.g., in the animal's home cage or during experiments.

Mice implanted with a Hybrid Drive targeting the hippocampal CA1 region readily explored the environment while enabling recordings from large numbers cells in the CA1 pyramidal layer together with local field potentials (LFPs) from all CA1 layers (Figures 1E,F) during a variety of behavioral paradigms (Movie S1).

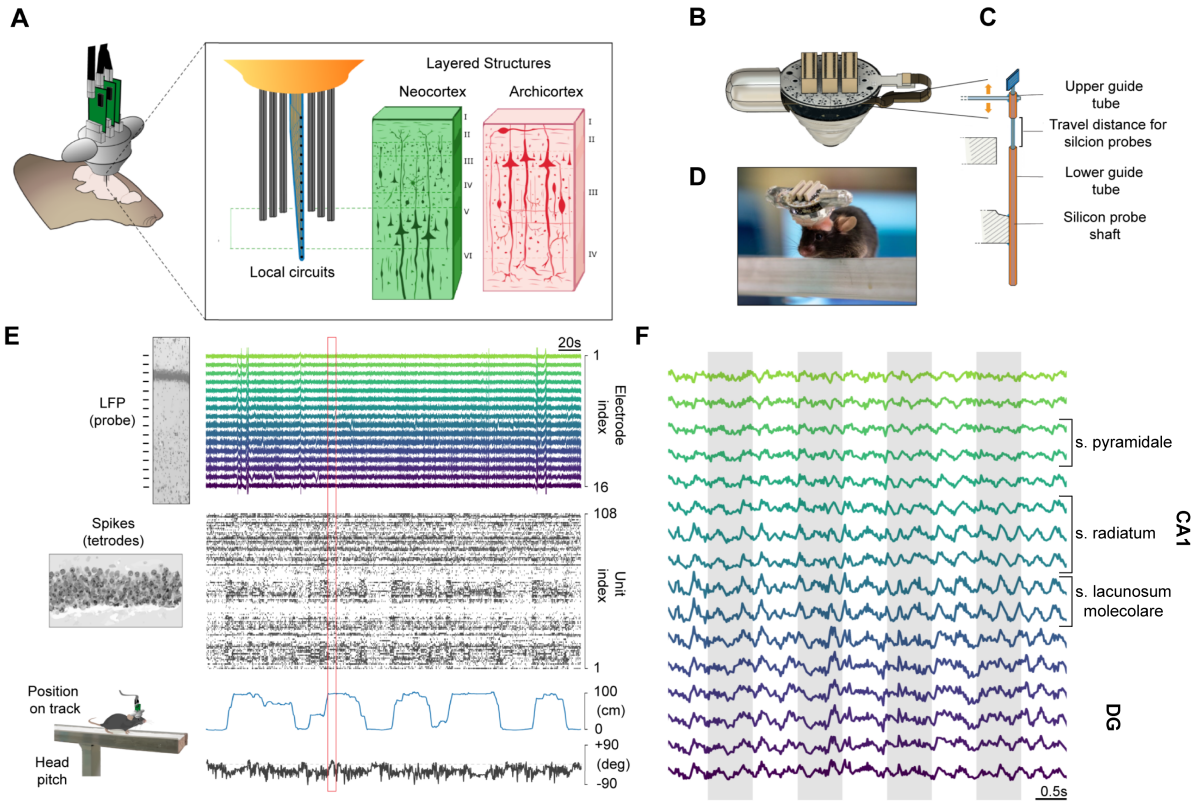

Figure 1: **Simultaneous measurement of within-layer and across-layer electrophysiological activity in a freely moving mouse.** (A) Neural activity is recorded using a chronic implantable "Hybrid Drive" that contains 14 tetrodes and 1–2 silicon probes. The silicon probes record neural activity across layers of a given structure, while tetrodes can record activity of single cells from within a single layer. (B) 3D model of a fully-assembled Hybrid Drive. Lateral plastic cone shields protect the flex cables and ZIF connectors of the silicon probes. (C) Illustration of the spring-screw mechanism enabling independently movable silicon probes and tetrodes. (D) Photo of the Hybrid Drive implanted in a 5 month old C57BL6/J mouse. (E) Example traces of neural and behavioral variables simultaneously recorded with the Hybrid Drive in an animal traversing a linear track. Top: Local field potential (LFP) recordings from the silicon probe, spanning dorsal CA1. Middle: raster plot of single units recorded with tetrodes in the CA1 pyramidal layer. Bottom: head pitch and the animal's position on the linear track. (F) Zoomed-in LFP traces for the region marked by the red rectangle in E. LFP traces show typical markers of CA1 layers, including depth-dependent oscillation amplitude and theta phase reversal in deeper layers. Shaded gray regions for easier visualization of temporal alignment.

The Hybrid Drive enables stable recordings of neural activity across weeks

We first checked that the presence of the silicon probe did not interfere with the quality of concomitant tetrode recordings (and vice versa; Figure 2). To quantify recording quality, the tetrodes of the Hybrid Drive were implanted in the pyramidal layer of dorsal CA1 while the linear silicon probe spanned the entire CA1 region, orthogonal the pyramidal layer (Figure 1E). Recordings were performed in three animals in a variety of tasks across at least 20 days. For each animal, experimental day 1 started when the majority of tetrodes exhibited sharp wave ripple (SWR) complexes during rest sessions in the home cage or clearly discernible theta oscillations during locomotion.

Well-isolated single units could consistently be recorded across weeks (Figure 2B). The number of isolated units was slightly lower on the first recording days, potentially resulting from uncertainty in positioning the tetrode tips in the pyramidal layer. Fine adjustments of the depths of individual tetrodes enabled the precise placement of tetrodes in the pyramidal layer ($\approx$ 80 microns thickness) to maximize the yield of simultaneously recorded cells.

To test the quality of detected spikes, we estimated signal-to-noise (SNR) measures (Meyer et al., 2018, Magland et al., 2020) for each tetrode channel for different recording days. Across all three animals, SNR increased across days (Figure 2C). We wondered if these changes in SNR across days can be explained by changes in behavior. To test this, we segmented the data into "Active" and "Quiescent" periods based on signals measured using the head-mounted accelerometer (Meyer et al., 2018) and computed SNR values for

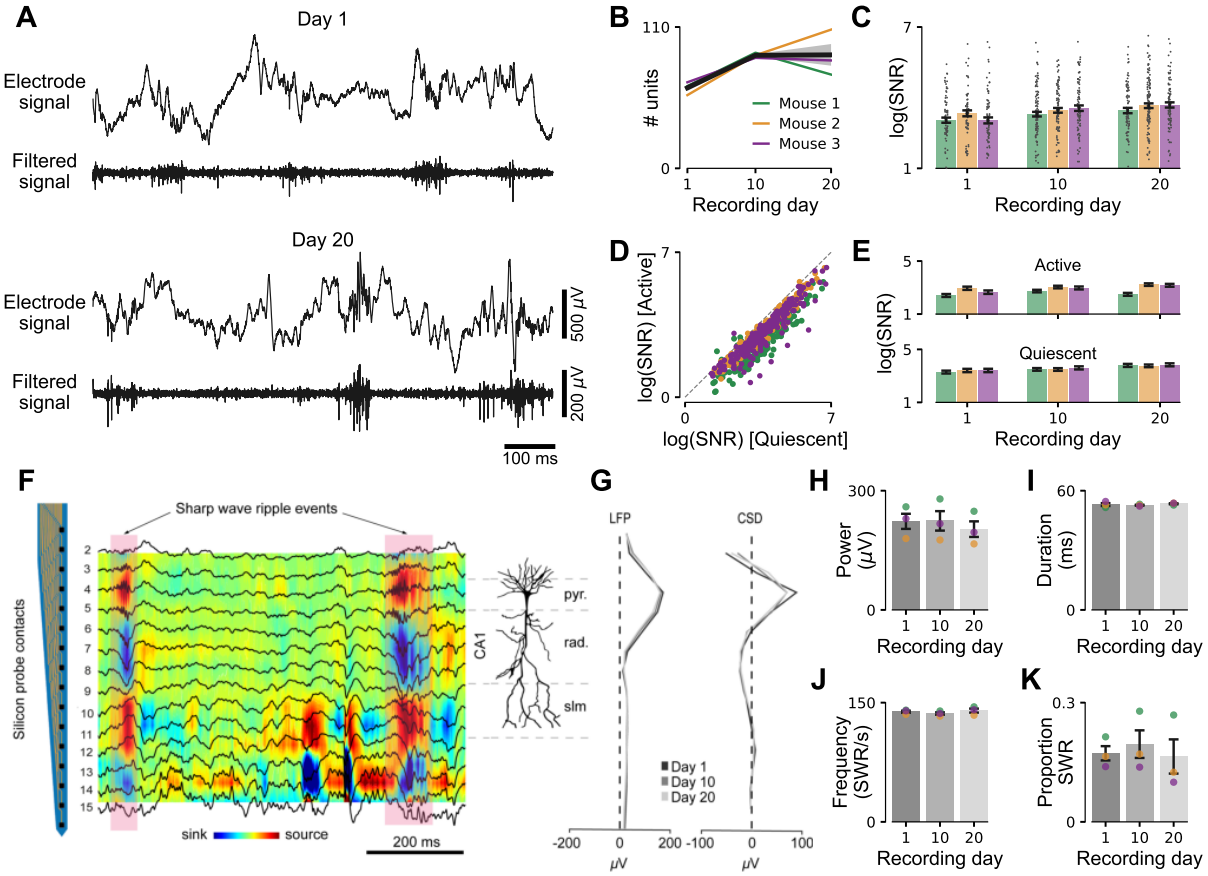

Figure 2: **Neural recording quality is not affected when combining tetrodes with silicon probe recordings.** (A) Broadband electrode signal from an example tetrode channel and high-pass filtered signal for the same channel on the first recording day (day 1; top) and 19 days later (day 20, bottom). (B) Number of isolated single units from 13 tetrodes positioned in the CA1 pyramidal layer for different recording days (mean day 1: 62.6 ± 5.1, mean day 10: 88 ± 2, mean day 20: 88.3 ± 17.8). Colors indicate different animals. (C) Signal-to-noise ratio (SNR) for different recording days. Gray dots indicate SNR estimates for single units. Same data as in B. Mean ± SEM. (D) SNR for different behavioral states (Active, Quiescent) pooled across days. Same data as in B. (E) The same as in C but separated into Active and Quiescent states. Increases in SNR in the presence of silicon probes can not be explained by changes in behavior across days. (F) Current-source density (CSD) computed from silicon probe targeting different CA1 layers during a rest session in the animal's homecage. Superimposed LFP signals are aligned with CSD sink and sources. Silicon probe channels shown to the left. Example sharp wave ripple (SWR) events indicated by shaded red areas. (G) High-frequency oscillation (100-250 Hz) power profiles along the silicon probe for LFP (left) and CSD (right) signals. The profiles remain stable across days (Day 1, 10 and 20) with a clear peak in the pyramidal layer electrode. (H-K) SWR power, SWR duration, SWR frequency, and proportion of SWR events across recording days (during quiescent state). One home cage rest session per animal (each approx. 60 min).

each condition. While cells had a lower SNR during the "Quiescent" compared to the "Active" condition (Figure 2D), this difference in SNR could not explain changes in SNR within conditions across days (Figure 2E). This suggests that the Hybrid Drive can reliably record neural ensembles for an extended period, similar to what is know for standard tetrode implants (Voigts et al., 2013, 2020).

Finally, we investigated common electrophysiological markers to assess the recording quality of the chronically implanted silicon probe. We focused on sharp wave ripple (SWR), distinct oscillatory patterns in the LFP often associated with memory-related processes during sleep (Buzsaki et al., 2015, Fernández-Ruiz et al., 2019). Figure 2F shows unfiltered LFP signals exhibiting SWR events, together with the Current Sources Density (CSD) estimated from the LFP data. The SWR power depth profile maintained a consistent shape throughout the different weeks (Figure 2G, left). Similar results were found after applying CSD analysis to extract layer-independent oscillatory patterns (Figure 2G, right). The stability of the probe and the quality of the recorded signals were confirmed by multiple SWR measures. We found no significant differences in either SWR power (Figure 2H; One-way ANOVA, $p = 0.82$), SWR duration (Figure 2I; One-way ANOVA, $p = 0.69$), SWR frequency (Figure 2J; One-way ANOVA, $p = 0.55$) and proportion of detected SWR events (Figure 2J; One-way ANOVA, $p = 0.86$) between recording days 1, 10, and 20.

Patterns of behavior are minimally disturbed by the drive implant

Next, we investigated the impact of the Hybrid Drive implant on gross locomotor and exploratory animal behavior. Previous work has shown that mice tolerate tetrode implants such as the flexDrive with only minimal changes in natural behavior (Voigts et al., 2013, Meyer et al., 2018, Voigts et al., 2020). To test if this is also true for the Hybrid Drive with the addition of silicon probes, we first analyzed locomotion patterns of mice traversing a linear track (Figure 3A). Animals received a reward at the ends of the track every time they completed a full lap (end-to-end run). Even without food deprivation, animals learned to consistently move from one end to the other to receive a reward; their running behavior became more stereotypical with increasing numbers of laps across days (Figure 3B). This increase was consistent across animals (Figure 3C) and was statistically significant in two of the three animals (Mouse 1, +2.1 laps per day, $p = 0.03$; Mouse 2, +2.6 laps per day, $p = 0.004$; Mouse 3, +1.7 laps per day, $p = 0.48$; Wald Test on slope of the linear fit). Mice were also running faster as indicated by the change in the running speed profile (Figure 3D; permutation test days 1–5 vs days 6–10, $p = 0.029$).

We examined more closely the potential effects of the size and weight of the drive on the behavior of an example mouse, paying attention to head movements across days (Figure 3E). Starting from recording day 5 on the linear track, the mouse was holding its head more closer to its natural position (typical pitch $\approx$ -25 deg; Meyer et al. (2018)). On day 10, we observed a decrease in variability, potentially resulting from more stereotypical running (day 1, pitch -34.9 ± 14.4 deg, roll 2.2 ± 8.7 deg; day 5, pitch -28.6 ± 15.3 deg, roll 3.1 ± 9.0 deg; day 10, pitch -28.7 ± 11.5 deg, roll 2.7 ± 9.5 deg).

Finally, we compared exploratory behaviors in two-dimensional environments that contained a small number of objects. Animals were free to explore a square environment (width: 75 cm) for 10 minutes. This was repeated on the same recording day to yield 5–7 consecutive trials per animal per day. We tracked the animal's positions from camera recordings using a convolutional deep neural network trained using transfer learning (Mathis et al., 2018). To obtain baseline measures of animals with a slightly more lightweight neural implant ($\approx$ 2 grams) without silicon probes, we implanted three animals with a flexDrive (Voigts et al., 2013).

We found no difference in exploration patterns between animals implanted with a Hybrid Drive or a more lightweight flexDrive. Animals spent similar amounts of time close to objects (Figure 3G; Wilcoxon rank-sum test, $p = 0.17$) and visited a comparable number of objects during a trial (Figure 3H; Wilcoxon rank-sum test, $p = 0.099$). There was also no discernible difference in object exploration duration (Figure 3I; permutation tests, $p = 0.17$) and in body speed (Figure 3J; permutation tests, $p = 0.23$).

We conclude that learning of goal-directed behaviors and the ability to explore, and interact with, more complex environments were minimally affected by the presence and additional weight of the silicon probes.

Interactions of spiking and across-layer neural activity vary with behavioral state in freely moving mice

We next explored the capacity of the Hybrid Drive to identify interactions between the spiking activity of single cells and across-layer LFP signals during different behaviors. Animals that can freely interact with their environments show a wide range of behaviors, including active exploration, quiescence, and sleep (Krakauer et al., 2017). To identify neural correlates of these behavioral "states", mice implanted with a Hybrid Drive in CA1 were free to explore a rectangular open field arena (Figure 4A). Behavioral

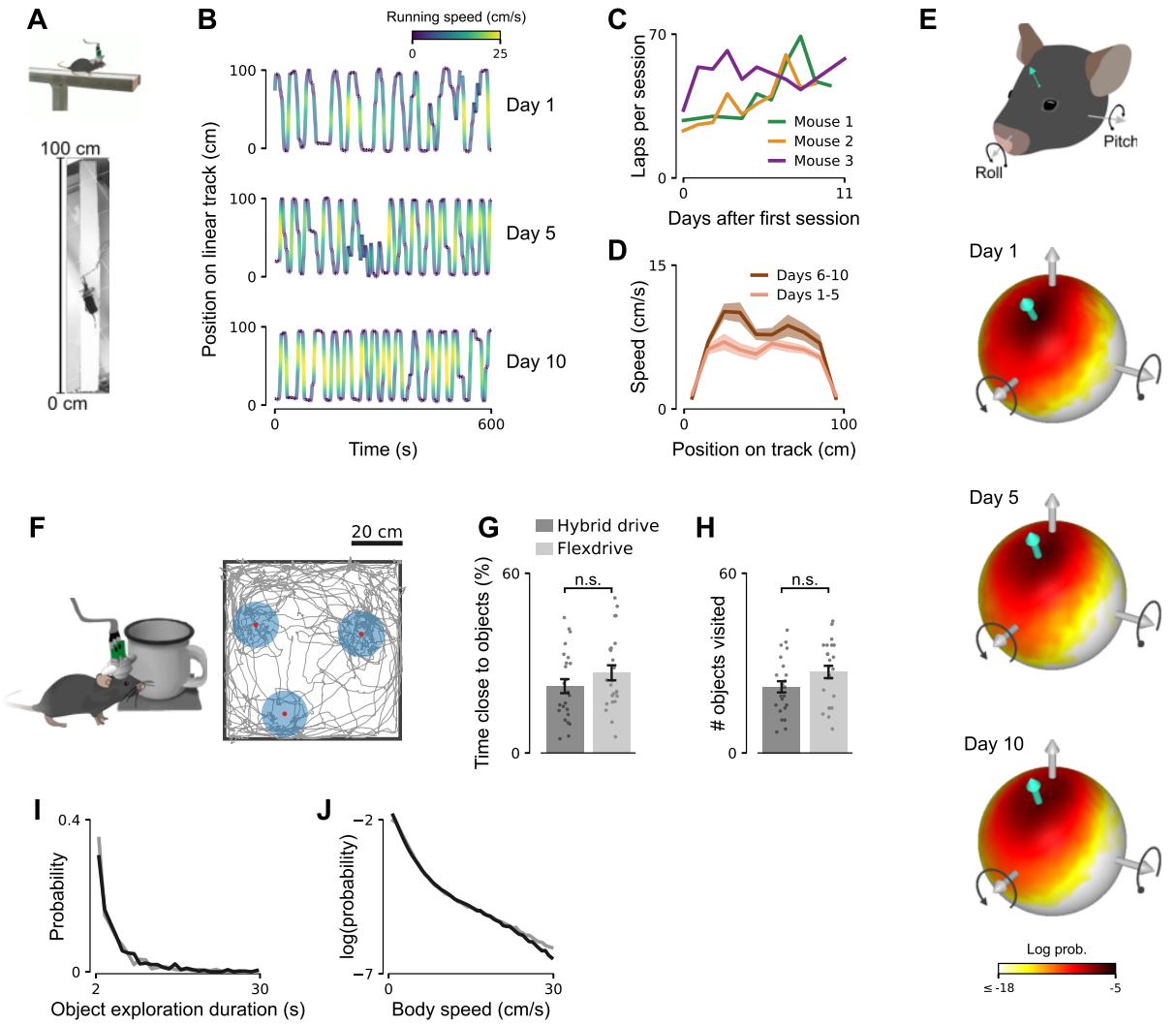

Figure 3: **Patterns of behavior are minimally disturbed by the drive implant.** (A) Mice implanted with a Hybrid Drive learned to traverse a linear track to receive rewards provided at the ends of the track. (B) 10-min example segments from different recording days (1, 5, and 10). Even without food deprivation, mice show increasingly stereotypical running behavior. Color denotes running speed. (C) Number of laps (end-to-end runs) per session. Data from three animals (n=9, 10, 10 sessions in mouse 1 (19.25 ± 4.04 minutes), 2 (29.15 ± 5.75 minutes), and 3 (25.17 ± 4.68 minutes), respectively). (D) Average running speed profiles for early (days 1–5, black line) and late (days 6–10, gray line) recordings. Mean $\pm$ SEM. Same data as in B. (E) Log-probability distribution of head tilt for day 1 (top), 5 (middle), and day 10 (bottom) for the data shown in C (mouse 1). Illustration indicates pitch and roll axes. Turquoise arrow indicates mean orientation of vertical (ventral-dorsal) head axis. (F) Object exploration task in which mice are freely exploring three objects in a square arena (width = 75cm). Red dots indicate object centers. Shaded blue circles (radius = 10 cm) show the area around each object that was considered as close to the object. Gray line indicates position of the mouse's head in the arena for a 10-min trial. (G) Time close to objects for animals implanted with a Hybrid Drive (dark gray) or a flexDrive (light gray). Dots show single trials (10 min each). Number of trials: Hybrid Drive, n=7, 12, 5 trials in mouse 1, 2, 3, respectively; Flex drive, n=12, 6, 6 trials in mouse 4, 5, 6, respectively. Mean $\pm$ SEM. (H) Number of objects visited per trial. Mean $\pm$ SEM. Same data as in G. (I) Distribution of object exploration duration. Same data as in G. (J) Log-scaled distribution of body speed for animals implanted with a Hybrid Drive or flexDrive. Same data as in G.

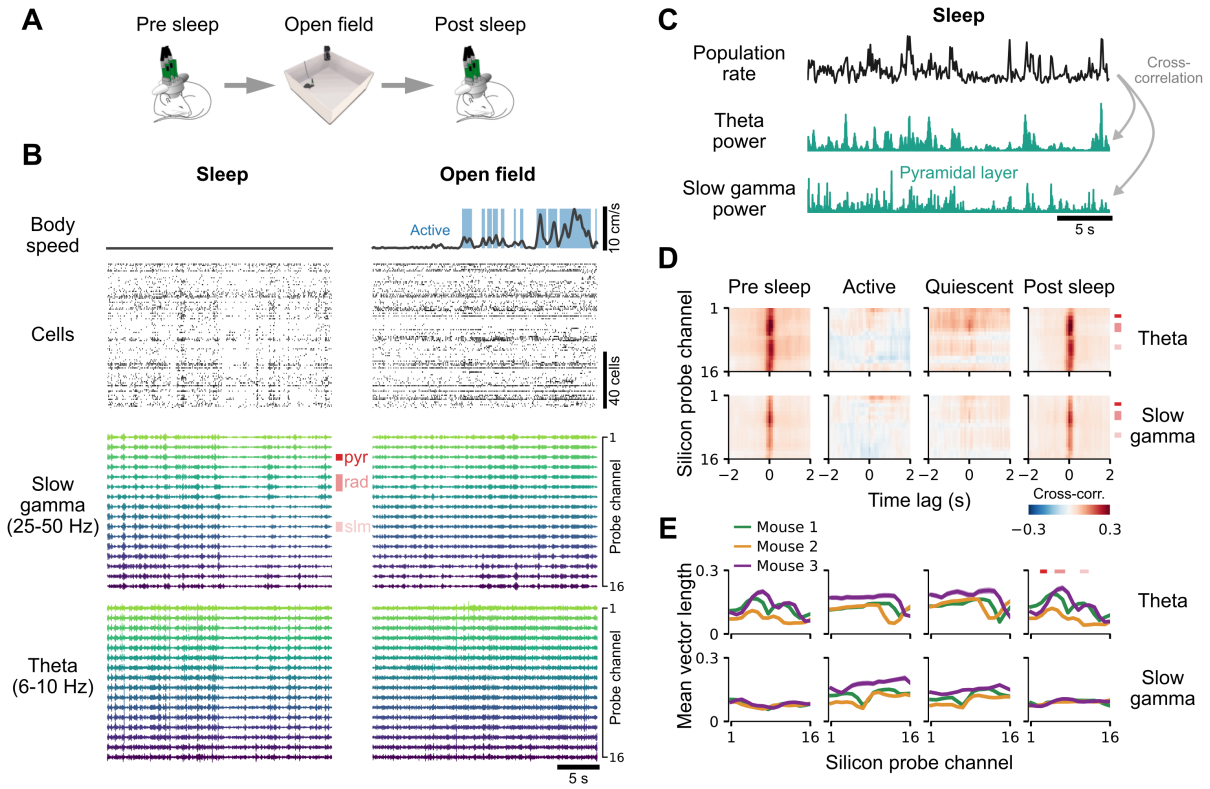

Figure 4: **Interactions of spiking and across-layer neural activity vary with behavioral state in freely moving mice**. (A) Neural activity and behavioral variables were measured while an animal was either sleeping or freely exploring an open field environment. (B) Example traces of simultaneously measured behavioral and neural variables for sleep (left) and open field exploration (right). Blue shaded regions in body speed trace indicate "Active" periods (body speed $\geq$ 2 cm/s). All other periods were considered as "Quiescent". Vertical red bars indicate locations of pyramidal (pyr), radiatum (rad), and slm layers relative to the silicon probe electrodes. (C) Population rate and LFP power in the theta and slow gamma frequency bands for the silicon probe electrode in the pyramidal layer for the sleep data in B. The population rate was computed as the average rate across all cells in 100 ms bins. (D) Cross-correlation between the population rate and silicon probe LFP power for different behavioral states. Top row shows results for theta LFP power and bottom row for slow gamma LFP power. Vertical red bars indicate locations of CA1 layers as in B. Same recording as in B. (E) Mean vector length of phase locking between spike times of single cells and LFP phase. Mean $\pm$ SEM (smaller than line width). Columns show the same conditions as in D. Line colors indicate different animals. Horizontal red bars indicate locations of CA1 layers as in B and D.

variables were measured using an external video camera and the head-mounted accelerometer. Before and after the open field recording, mice were allowed to naturally transition to sleep in their home cages while we recorded from the same cells as in the open field condition. Segmenting the open field recording into "Active" (body speed $\geq$ 2 cm/s) and "Quiescent" (body speed $<$ 2cm/s) periods using video data allowed us to compare neural activity across four different conditions: "Pre sleep", "Active", "Quiescent", and "Post sleep". To exclude movement periods during the home cage sleep condition, we focused on periods during which mice were not moving their heads or bodies.

Figure 4B shows 30 s extracts of movement signals, spiking activity, slow gamma (25–50 Hz) and theta (6-10 Hz) band LFP signals for a sleep and subsequent open field recording for an example animal. During sleep, spiking activity and LFP signals across all layers showed strong co-fluctuations, possibly reflecting cortical up and down states (Battaglia et al., 2004). These co-fluctuations extended across all probe layers but were not present in the "Active" or the "Quiescent" open field conditions. To test if this is true for the whole recording, we computed the cross-correlation between the population spike rate (defined as the sum across all cells in 100 ms second bins) and the power in the different LFP channels (Figures 4C,D). Cross correlations extended across all silicon probe electrodes and were strongest close to the pyramidal layer from which the single cells were recorded (Figure 4D). In contrast, cross-correlations were largely absent in the "Active" state and confined to the stratum radiatum in the "Quiescent" state of the open field recording. This effect did not depend on LFP power as this was generally stronger during

open field recordings and firing rates of single cells were also higher during the active state (Figure S4). Thus, on a population level, spiking activity and LFP power show distinct behavioral state-dependent patterns across different CA1 layers.

We further asked if the association of the firing of single spikes to the phase of LFP oscillations on a millisecond time scale (phase locking) might exert a similar depth dependence. In contrast to the population activity, there was discernible phase locking patterns across all layers and conditions (Figure 4E). The dependency on LFP probe channel was largely consistent between pre and post sleep conditions for the theta band (permutation tests; $p > 0.5$ for all mice), exhibiting a clear peak in the stratum radiatum, but differed significantly for slow gamma (permutation tests; $p < 0.001$ for all mice). However, the depth-dependence of theta band phase locking was significantly different between the active and sleep conditions (permutations tests; $p < 0.001$ for all conditions for each mouse; Bonferroni correction).

These results demonstrate that the Hybrid Drive enables a detailed characterization of the relationship between layer-specific and across-layer neural activity during different behaviors in freely moving mice.

Across-layer information improves prediction accuracy of CA1 pyramidal layer cell responses

We next investigated how multiple behavioral variables and neural activity across different hippocampal layers contribute to the firing of single cells within the CA1 pyramidal layer. CA1 pyramidal cells show selectivity to different behavioral variables, including the animal's position, head direction, and running speed (O'Keefe and Dostrovsky, 1971, McNaughton et al., 1983, Muller et al., 1994, Skaggs and McNaughton, 1998, Knierim, 2002). At the same time, CA1 cells can be coupled to internal network state, in particular by firing in relation to theta oscillations (Skaggs et al., 1996, Csicsvari et al., 1999, Mizuseki et al., 2011). To simultaneously characterize selectivity of single CA1 cells to multiple behavioral variables and theta activity, we adapted a generalized linear model (GLM) with Poisson response distribution (Figure 5A) (Burgess et al., 2005, Acharya et al., 2016, Hardcastle et al., 2017). A major advantage of a GLM-based approach over traditional tuning curves is its robustness to the interdependence of encoded variables which can lead to bias when analyzing the impact of these variables separately (Hardcastle et al., 2017, Stevenson, 2018, Laurens et al., 2019). For each cell, a GLM was trained to predict the cell's firing in 100 ms bins using the animal's position on the linear track, head direction, and running velocity (where positive/negative velocity corresponds to the animal running to the far/near end of the track). Additionally, we included neural variables derived from the chronic silicon probe in the Hybrid Drive: theta (6–10 Hz) LFP amplitude extracted from either the electrode in the pyramidal layer (in which the tetrodes were positioned) or from all CA1 electrodes (Figure 5A, bottom right). The latter allows for integration of across-layer information which cannot be captured by the tetrodes alone.

Many CA1 pyramidal layer cells showed tuning to multiple behavioral variables and theta amplitude at different depths (Figures 5B,C). To determine the significant GLM weights for each variable, we also computed weights for the same model (i.e. the same hyperparameters) after shuffling the spike train for each neuron; significant GLM weights were defined as those that exceeded 3 standard deviations of the shuffled weights ($n = 1000$ shuffles). Significant theta amplitude weights were generally large for silicon probe electrodes in the stratum pyramidal, stratum radiatum and stratum lacunosum moleculare ("pyr", "rad", and "slm" in Figures 5B,C). This observation was consistent across animals (Figure 5D). Importantly, inclusion of across-layer theta power signifcantly improved cross-validated prediction accuracy compared to a GLM with only pyramidal layer theta amplitude (Figure 5E; Wilcoxon signed-rank test; mouse 1, $p = 0.034$; mouse 2, $p = 4.2 \cdot 10^{-5}$; mouse 3, $p = 5.5 \cdot 10^{-5}$).

We conclude that across-layer LFP signals provide additional information for single cells that is not captured by behavioral variables and the LFP signal within the pyramidal layer alone. Moreover, the consistent structure of theta GLM weights across mice support the idea that theta oscillations in the pyramidal, radiatum, and slm layers provide distinct afferent inputs to pyramidal layer cells (Schomburg et al., 2014, Lasztóczi and Klausberger, 2014).

Discussion

Here we present the Hybrid Drive, a chronic implant device combining tetrode arrays with silicon probes in freely moving mice. A key feature of the drive is its flexibility: the arrangements of tetrodes and silicon probes can easily be adapted depending on the brain areas under investigation, opening up new avenues in studying the relation between layer-specific and across-layer neural activity, with high spatial and temporal precision. The drive is light enough to study a wide range of naturalistic behaviors; this includes standard paradigms such as running on a linear track (Figure 3) and open field exploration (Figure 4) but also interactions with objects in the environment (Figure 3) and, importantly, natural transition to

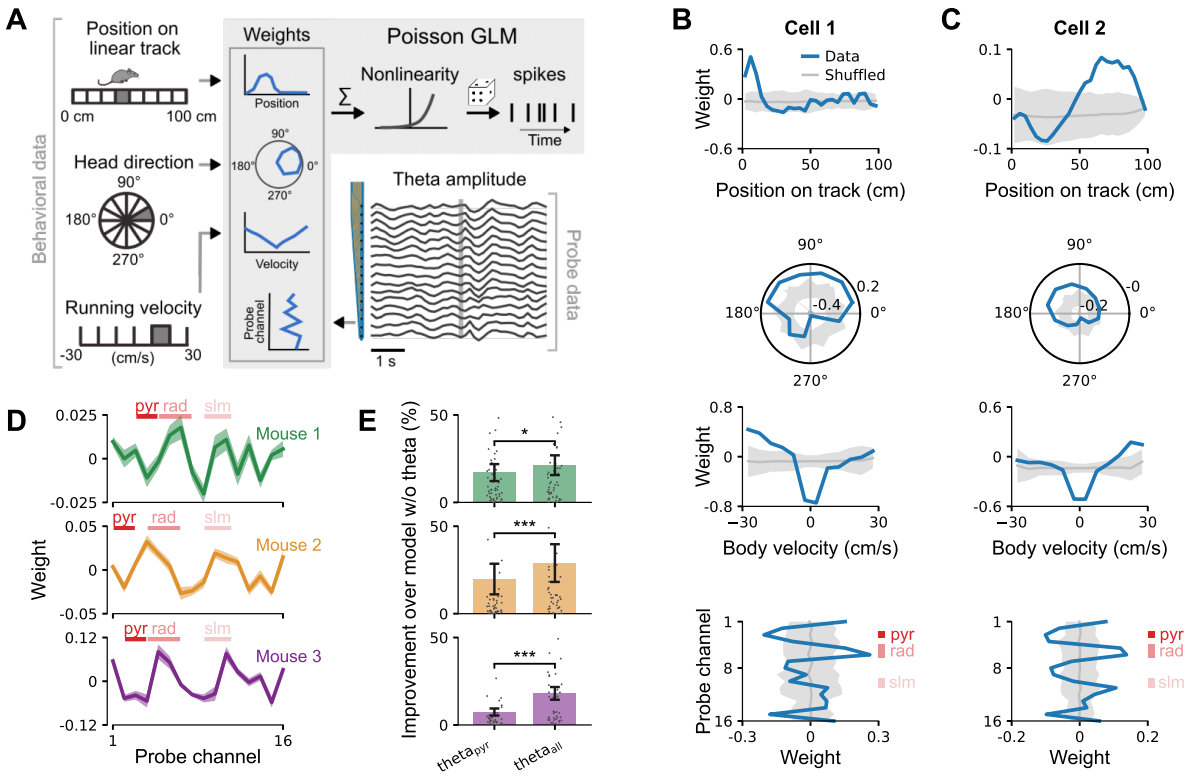

Figure 5: **Across-layer information improves prediction accuracy of CA1 pyramidal layer cell responses**. (A) Behavioral variables and silicon probe data were used to fit the parameters of a Poisson Generalized Linear Model (GLM) to predict the response of simultaneously recorded pyramidal layer cells. The gray bin indicates the current value. For probe data, the vertical gray line indicates the current theta band (6–10 Hz) LFP amplitudes. Position on track and running velocity bin counts reduced for illustration purposes. (B) Fitted GLM weights for an example CA1 pyramidal layer cell recorded using the tetrodes in the Hybrid Drive. Solid blue lines show weights of model fitted on the measured spike train. Gray line and shaded gray area show mean and 3 SD of shuffled spike train, respectively ($n = 1000$ shuffles). Vertical red bars in bottom plot indicate locations of pyramidal, radiatum, and slm layers relative to the silicon probe electrodes. (C) The same as in B for another example cell. (D) Summary of theta amplitude GLM weights for three animals. Horizontal red bars indicate locations of CA1 layers relative to the silicon probe electrodes as in B and C. Positive (negative) weights correspond to an increase (decrease) in single-cell firing and are consistent for pyramidal layer, radiatum and slm across mice. Mean ± SEM across cells for each animal (mouse 1: 50 cells, mouse 2: 46 cells, mouse 3: 41 cells). Only cells with a firing rate of at least 2 spikes/s were included in the analysis. (E) Prediction performance of a GLM that includes theta amplitudes from all silicon probe electrodes ($\text{theta}_{\text{all}}$) compared to a GLM that only includes theta LFP amplitude for the electrode in the pyramidal layer ($\text{theta}_{\text{pyr}}$). Improvement based on cross-validated predictions (4 folds) relative to a model without silicon probe data. Dots indicate single cells for the same data as in D. Wilcoxon signed-rank test, *p < 0.05, ***p < 0.0001. Mean ± SEM.

sleep (Figure 4). The latter plays a crucial role in memory research and is generally challenging to study in head-restrained mice in which large-scale neural recordings techniques are readily available (Steinmetz et al., 2019).

Layer-resolved oscillations provide unique information about different input streams to a cortical module, and about its internal processes. The hippocampus is one of the brain regions where the functional connectivity and the link to oscillatory phenomena are best known (Schomburg et al., 2014), but the analysis has been successfully applied to the neocortex as well (Kerkoerle et al., 2014). In CA1, for example, research has shown that theta oscillations result from the combination of inputs feeding to different layers (Buzsáki, 2002). "Gamma oscillations" have also been shown to be an umbrella term that encompasses multiple phenomena and generating circuits, which may be differentiated by frequency (Bragin et al., 1995, Colgin et al., 2009), but even more precisely when layer localization is added (Lasztóczi and Klausberger, 2014). In this paper, we show how our Hybrid Drive may be used to study the association of neural ensemble firing with oscillatory patterns. For example, in Figure 4 we show how the correlations between population firing and LFP generators at different layers is affected differently by changes in behavioral state, with only the stratum radiatum retaining coherence outside of the sleep state (characterized by low-frequency driven high coherence throughout the layer; Figure 4D). Similarly, the phase locking pattern to theta and slow gamma show layer and behavioral state dependent effects (Figure 4E). For example, a clear peak in the stratum radiatum emerges in the sleep phase, which is absent during wakefulness.

Our results also show that the availability of the layer-specific LFP enables a better characterization of the coding properties of single hippocampal cells. A Poisson GLM including layer resolved theta power has significantly higher predictive power for cell firing compared to behavioral variables typically used in spatial coding (Hardcastle et al., 2017), with a distinctive pattern of layer contributions emerging (Figure 5). Interestingly, when predicting single-neuron firing, GLM weights for theta power change sign multiple times along the dorsoventral axis, suggesting differential roles of generators in different layers in firing neurons. We believe that this improved characterization may help shedding light on neural coding properties, for example in approaches including "neural" and "external" predictor variables as in our analysis.

The Hybrid Drive is open source and we provide all required design files along with detailed building instructions. The drive is based on a widely-used existing design (Voigts et al., 2013) which should further promote its adoption. Furthermore, the system is modular and could be combined with technologies for optogenetic manipulation of neural activity or miniature head-mounted cameras to capture detailed behavioral variables, such as whisking or eye movements (Meyer et al., 2018). Together with recent advances in marker-less tracking of specific body parts (Mathis et al., 2018) and analytical tools to analyze spike trains of neurons across brain areas (Grossberger et al., 2018, Keeley et al., 2020), the Hybrid Drive helps to increase the range of questions that can be addressed about the neural basis underlying natural behaviors in freely moving mice and other small laboratory animals.

Acknowledgments

We thank Bruce McNaughton, Oscar Chadney and Jan Klee for their comments on the manuscript and the Battaglia lab for helpful discussions and comments during different stages of this work. This work was supported by the Radboud Excellence Initiative (A.F.M.), the European Union's Horizon 2020 research and innovation program (MGate, grant agreement no. 765549; M.G. and F.P.B.), and the European Research Council (ERC) Advanced Grant "REPLAY-DMN" (grant agreement no. 833964; F.P.B.).

Author contributions

Conceptualization: M.G., A.F.M., and F.P.B.; Investigation and Data Curation: M.G.; Methodology and Software: M.G, R.E., R.P., and A.F.M; Resources: A.A. and F.P.B.; Formal Analysis and Visualization, M.G., R.P., and A.F.M.; Writing – Original Draft: M.G. and A.F.M; Writing – Review & Editing: M.G., A.F.M., and F.P.B.; Supervision and Funding Acquisition: A.F.M. and F.P.B.

References

Acharya, L., Aghajan, Z. M., Vuong, C., Moore, J. J., and Mehta, M. R. (2016). Causal influence of visual cues on hippocampal directional selectivity. *Cell*, 164:197–207.

Amaral, D. G. and Witter, M. P. (1989). The three-dimensional organization of the hippocampal formation: A review of anatomical data. *Neuroscience*, 31(3):571–591.

Andersen, P., Bliss, T., and Skrede, K. (1971). Lamellar organization of hippocampal excitatory pathways. *Experimental Brain Research*, 13(2).

Andersen, P., Morris, R., Amaral, D., Bliss, T., and O'Keefe, J. (2006). *The Hippocampus Book*. Oxford Neuroscience Series. Oxford University Press, New York.

Battaglia, F. P., Sutherland, G. R., and McNaughton, B. L. (2004). Hippocampal sharp wave bursts coincide with neocortical "up-state" transitions. *Learning & Memory*, 11:697–704.

Bragin, A., Jandó, G., Nádasdy, Z., Hetke, J., Wise, K., and Buzsáki, G. (1995). Gamma (40-100 Hz) oscillation in the hippocampus of the behaving rat. *The Journal of Neuroscience*, 15(1 Pt 1):47–60.

Burgess, N., Cacucci, F., Lever, C., and O'keefe, J. (2005). Characterizing multiple independent behavioral correlates of cell firing in freely moving animals. *Hippocampus*, 15:149–153.

Buzsaki, G., Stark, E., Berenyi, A., Khodagholy, D., Kipke, D. R., Yoon, E., and Wise, K. D. (2015). Tools for probing local circuits: High-density silicon probes combined with optogenetics. *Neuron*, 86(1):92 – 105.

Buzsáki, G. (2002). Theta Oscillations in the Hippocampus. *Neuron*, 33(3):325–340.

Chen, S., He, L., Huang, A. J. Y., Boehringer, R., Robert, V., Wintzer, M. E., Polygalov, D., Weitemier, A. Z., Tao, Y., Gu, M., Middleton, S. J., Namiki, K., Hama, H., Therreau, L., Chevaleyre, V., Hioki, H., Miyawaki, A., Piskorowski, R. A., and McHugh, T. J. (2020). A hypothalamic novelty signal modulates hippocampal memory. *Nature*, 586:270–274.

Colgin, L. L., Denninger, T., Fyhn, M., Hafting, T., Bonnevie, T., Jensen, O., Moser, M.-B., and Moser, E. I. (2009). Frequency of gamma oscillations routes flow of information in the hippocampus. *Nature*, 462(7271):353–357.

Csicsvari, J., Hirase, H., Czurko, A., Mamiya, A., and Buzsaki, G. (1999). Oscillatory Coupling of Hippocampal Pyramidal Cells and Interneurons in the Behaving Rat. *Journal of Neuroscience*, 19(1):274–287.

Delorme, A. and Makeig, S. (2004). Eeglab: an open source toolbox for analysis of single-trial eeg dynamics including independent component analysis. *Journal of Neuroscience Methods*, 134:9–21.

Deshmukh, S. S. and Knierim, J. J. (2011). Representation of non-spatial and spatial information in the lateral entorhinal cortex. *Frontiers in behavioral neuroscience*, 5:69.

Fernández-Ruiz, A., Oliva, A., Oliveira, E. F. d., Rocha-Almeida, F., Tingley, D., and Buzsáki, G. (2019). Long-duration hippocampal sharp wave ripples improve memory. *Science*, 364(6445):1082–1086.

Gothard, K. M., Skaggs, W. E., and McNaughton, B. L. (1996). Dynamics of mismatch correction in the hippocampal ensemble code for space: interaction between path integration and environmental cues. *The Journal of Neuroscience*, 16:8027–8040.

Grossberger, L., Battaglia, F. P., and Vinck, M. (2018). Unsupervised clustering of temporal patterns in high-dimensional neuronal ensembles using a novel dissimilarity measure. *PLOS Computational Biology*, 14(7):e1006283.

Hardcastle, K., Maheswaranathan, N., Ganguli, S., and Giocomo, L. M. (2017). A multiplexed, heterogeneous, and adaptive code for navigation in medial entorhinal cortex. *Neuron*, 94:375–387.e7.

Harris, K. D., Henze, D. A., Csicsvari, J., Hirase, H., and Buzsáki, G. (2000). Accuracy of tetrode spike separation as determined by simultaneous intracellular and extracellular measurements. *Journal of Neurophysiology*, 84(1):401–414.

Herwik, S., Paul, O., and Ruther, P. (2011). Ultrathin silicon chips of arbitrary shape by etching before grinding. *Journal of Microelectromechanical Systems*, 20(4):791–793.

Keeley, S. L., Zoltowski, D. M., Aoi, M. C., and Pillow, J. W. (2020). Modeling statistical dependencies in multi-region spike train data. *Current Opinion in Neurobiology*, 65:194–202.

Kerkoerle, T. v., Self, M. W., Dagnino, B., Gariel-Mathis, M.-A., Poort, J., Togt, C. v. d., and Roelfsema, P. R. (2014). Alpha and gamma oscillations characterize feedback and feedforward processing in monkey visual cortex. *Proceedings of the National Academy of Sciences*, 111(40):14332–14341.

Knierim, J. J. (2002). Dynamic interactions between local surface cues, distal landmarks, and intrinsic circuitry in hippocampal place cells. *The Journal of Neuroscience*, 22(14):6254–6264.

Krakauer, J. W., Ghazanfar, A. A., Gomez-Marin, A., MacIver, M. A., and Poeppel, D. (2017). Neuroscience Needs Behavior: Correcting a Reductionist Bias. *Neuron*, 93(3):480–490.

Lasztóczi, B. and Klausberger, T. (2014). Layer-Specific GABAergic Control of Distinct Gamma Oscillations in the CA1 Hippocampus. *Neuron*, 81(5):1126–1139.

Laurens, J., Abrego, A., Cham, H., Popeney, B., Yu, Y., Rotem, N., Aarse, J., Asprodini, E. K., Dickman, J. D., and Angelaki, D. E. (2019). Multiplexed code of navigation variables in anterior limbic areas. *bioRxiv*.

Luo, L., Callaway, E. M., and Svoboda, K. (2008). Genetic dissection of neural circuits. *Neuron*, 57:634–660.

Magland, J., Jun, J. J., Lovero, E., Morley, A. J., Hurwitz, C. L., Buccino, A. P., Garcia, S., and Barnett, A. H. (2020). Spikeforest, reproducible web-facing ground-truth validation of automated neural spike sorters. *eLife*, 9.

Mathis, A., Mamidanna, P., Cury, K. M., Abe, T., Murthy, V. N., Mathis, M. W., and Bethge, M. (2018). Deeplabcut: markerless pose estimation of user-defined body parts with deep learning. *Nature Neuroscience*, 21:1281–1289.

McNaughton, B. L., O'Keefe, J., and Barnes, C. A. (1983). The stereotrode: A new technique for simultaneous isolation of several single units in the central nervous system from multiple unit records. *Journal of Neuroscience Methods*, 8(4):391–397.

Meyer, A. F., Poort, J., O'Keefe, J., Sahani, M., and Linden, J. F. (2018). A head-mounted camera system integrates detailed behavioral monitoring with multichannel electrophysiology in freely moving mice. *Neuron*, 100(1):46–60.

Mizuseki, K., Diba, K., Pastalkova, E., and Buzsáki, G. (2011). Hippocampal CA1 pyramidal cells form functionally distinct sublayers. *Nature Neuroscience*, 14(9):1174–1181.

Muller, R., Bostock, E., Taube, J., and Kubie, J. (1994). On the directional firing properties of hippocampal place cells. *The Journal of Neuroscience*, 14(12):7235–7251.

O'Keefe, J. and Dostrovsky, J. (1971). The hippocampus as a spatial map. Preliminary evidence from unit activity in the freely-moving rat. *Brain Research*, 34(1):171–175.

Oliphant, T. E. (2007). Python for scientific computing. *Computing in Science & Engineering*, 9(3):10–20.

Rossant, C., Kadir, S. N., Goodman, D. F. M., Schulman, J., Hunter, M. L. D., Saleem, A. B., Grosmark, A., Belluscio, M., Denfield, G. H., Ecker, A. S., Tolias, A. S., Solomon, S., Buzsaki, G., Carandini, M., and Harris, K. D. (2016). Spike sorting for large, dense electrode arrays. *Nature Neuroscience*, 19:634–641.

Schomburg, E. W., Fernández-Ruiz, A., Mizuseki, K., Berényi, A., Anastassiou, C. A., Koch, C., and Buzsáki, G. (2014). Theta phase segregation of input-specific gamma patterns in entorhinal-hippocampal networks. *Neuron*, 84:470–485.

Siegle, J. H., López, A. C., Patel, Y. A., Abramov, K., Ohayon, S., and Voigts, J. (2017). Open Ephys: an open-source, plugin-based platform for multichannel electrophysiology. *Journal of Neural Engineering*, 14(4):045003.

Skaggs, W. E. and McNaughton, B. L. (1998). Spatial Firing Properties of Hippocampal CA1 Populations in an Environment Containing Two Visually Identical Regions. *Journal of Neuroscience*, 18(20):8455–8466. Publisher: Society for Neuroscience Section: ARTICLE.

Skaggs, W. E., McNaughton, B. L., Wilson, M. A., and Barnes, C. A. (1996). Theta phase precession in hippocampal neuronal populations and the compression of temporal sequences. *Hippocampus*, 6(2):149–172.

Steinmetz, N. A., Aydin, C., Lebedeva, A., Okun, M., Pachitariu, M., Bauza, M., Beau, M., Bhagat, J., Böhm, C., Broux, M., Chen, S., Colonell, J., Gardner, R. J., Karsh, B., Kloosterman, F., Kostadinov, D., Mora-Lopez, C., O'Callaghan, J., Park, J., Putzeys, J., Sauerbrei, B., van Daal, R. J. J., Vollan, A. Z., Wang, S., Welkenhuysen, M., Ye, Z., Dudman, J. T., Dutta, B., Hantman, A. W., Harris, K. D., Lee, A. K., Moser, E. I., O'Keefe, J., Renart, A., Svoboda, K., Häusser, M., Haesler, S., Carandini, M., and Harris, T. D. (2021). Neuropixels 2.0: A miniaturized high-density probe for stable, long-term brain recordings. *Science*, 372.

Steinmetz, N. A., Zatka-Haas, P., Carandini, M., and Harris, K. D. (2019). Distributed coding of choice, action and engagement across the mouse brain. *Nature*, 576(7786):266–273.

Stevenson, I. H. (2018). Omitted variable bias in glms of neural spiking activity. *Neural Computation*, 30:3227–3258.

Voigts, J., Newman, J. P., Wilson, M. A., and Harnett, M. T. (2020). An easy-to-assemble, robust, and lightweight drive implant for chronic tetrode recordings in freely moving animals. *Journal of Neural Engineering*, 17:026044.

Voigts, J., Siegle, J. H., Pritchett, D. L., and Moore, C. I. (2013). The flexdrive: an ultra-light implant for optical control and highly parallel chronic recording of neuronal ensembles in freely moving mice. *Frontiers in Systems Neuroscience*, 7:8.

Wilson, M. A. and McNaughton, B. L. (1993). Dynamics of the hippocampal ensemble code for space. *Science*, 261:1055–1058.

Materials and Methods

Ethics statement

In compliance with Dutch law and institutional regulations, all animal procedures were approved by the Central Commissie Dierproeven (CCD) and conducted in accordance with the Experiments on Animals Act (project number 2016–014 and protocol numbers 0021 and 0029).

Animals

7 male C57BL6/J mice (Charles River) were used in this study. 4 animals were implanted with a Hybrid Drive. Another 3 animal were implanted with a flexDrive for the object exploration experiment. All animals received the implant between 12 and 16 weeks of age. After surgical implantation, mice were individually housed on a 12-h light-dark cycle and tested during the light period. Water and food were available *ad libitum*.

Probe fabrication

The flexibility of the silicon probes is an important feature that makes the current design of the drive possible. The silicon probes used in this study have been designed and fabricated by ATLAS Neuroengineering BV (Leuven, Belgium). The fabrication is done on 4 inch silicon wafers using standardized fabrication techniques established using micro-electromechanical systems engineering. First, a stress-compensated passivation stack of silicon oxide and silicon nitride is deposited and acts as an electrical insulator between the probe metallization and the underlying bulk silicon substrate. Next, the metallization is sputter deposited and patterned using a lift-off process. A second passivation layer has been deposited which protects the metallization against the cerebral fluids in the brain tissue. The passivation layer stack is patterned by reactive ion etching to expose the electrode contacts along the probe shaft and the bonding pads on the probe base. The electrode metallization layer is deposited and patterned using a lift-off technique, resulting in electrodes with surface area of $225\mu m^2$ made of iridium oxide. Following the definition of the electrodes, the passivation and insulation layers are patterned using reactive ion etching to define the probe outline and exposing the build silicon substrate. Next, trenches with vertical sidewalls are etched into the bulk silicon substrate using deep reactive ion etching followed by a wafer thinning process to end up with $50\mu m$ thin silicon probes. Finally, the probes are assembled with the highly flexible PI ribbon cable using a flip-chip bonding process.

Hybrid Drive Assembly

All parts and steps required to build a Hybrid Drive are summarized in a separate step-by-step protocol (`https://github.com/MatteoGuardamagna/Hybrid_drive`). Briefly, the drive mechanism of the Hybrid Drive is based on an existing design (flexDrive, Voigts et al. (2013)). Tetrodes were made from HM-L coated 90% platinum/10% iridium 12.5 μm diameter wire (California Fine Wire, USA). The guide arrays containing the tetrodes were assembled by building up layers of polyimide tubes, according to the target areas, and fixing them with epoxy resin (Araldite Rapid, Araldite, UK). For the silicon probe used in this study (E16R_60_S1_L20_NT with 60 µm pitch between contacts, ATLAS Neuroengineering, Belgium), a different polyimide tubing size was used to position the probes in the guide array. We used a 5x3 array design to cover the dorsal CA1 area along its proximo-distal axis (Figure S1A) Other array designs were successfully tested, including bilateral prefrontal cortex (Figure S1B). The spring-screw mechanism of the flexDrive allowed precise positioning and re-positioning of individual tetrodes (Figures S2B,C). This mechanism has been adapted and implemented in the Hybrid Drive to allow for independently movable silicon probes (Figure S2D). First, the portion of polyimide tubing that will create the upper guide tube must be slid along the silicon probe shaft. The length difference between the upper and lower guide tube determines the total travel distance of the probe (the maximum recommended distance is 2 mm; Figures S2A,D). After positioning each tetrode guide tube in the slots of the drive body, the silicon probes were inserted in the corresponding lower guide tubes. Finally, The EIB was glued to the drive body using epoxy resin and the silicon probes' ZIF plugs were inserted into the ZIF connectors on the EIB. The current version of the EIB (Figure S3) contains two 16 channel ZIF connectors. The flexible cables of the silicon probes were protected using lightweight cone shields attached to opposite ends of the EIB (Figure 1A).

Surgical Procedures

All surgeries were performed on experimentally-naive mice. Mice were anaesthetized with 1.25% – 2% isoflurane and injected with analgesia (Carprofen, 5 mg/kg SC). Mice were placed in a stereotaxic frame and antibacterial ophthalmic ointment (Alcon, UK) was applied to the eyes. A circular piece of dorsal scalp was removed and the underlying skull was cleaned and dried. 3 stainless steel M0.8 screws were used to secure the drive (1 ground screw in the frontal plate, 1 screw in the parietal plate opposite to micro-drive, 1 screw in the occipital plate). A craniotomy was made over the right cortex (top-left corner at AP: -1.20 mm; ML: 0.6 mm relative to bregma; bottom-right corner at AP: -2.30 mm; ML: 2.10 mm relative to bregma) using a 0.9 Burr drill. The dura was removed and the array of the drive was slowly lowered into the brain with the silicon probe shaft already adjusted at the final depth ($\approx$ 2.1 mm; Figure S1A). The guide tube array was lowered $\approx$ 0.5 mm above the brain surface and the craniomoty was filled with sterile vaseline to protect the brain and the array from cement flowing in. The drive was cemented onto the skull using dental adhesive (Superbond C&B, Sun Medical, Japan) and tetrodes were individually lowered into the brain (approx. 1 mm) using the screw-spring mechanism. Mice were allowed to recover from surgery for at least seven days before experiments began.

Neural and behavioral data collection

From post-surgery day 3 onward, animals were brought to the recording room and electrophysiological signals were investigated during a rest session in the home cage. Tetrodes were lowered in 45/60μm steps until common physiological markers for the hippocampus were discernible (SWR complexes during sleep or theta during locomotion). The majority of the tetrodes reached the target location (CA1 pyramidal layer) in 7-10 days. Silicon probe signals were used as additional depth markers.

Electrophysiological data were recorded with an Open Ephys acquisition board (Siegle et al., 2017). Signals were referenced to ground, filtered between 1 and 7500 Hz, multiplexed, and digitized at 30 kHz on the headstages (RHD2132, Intan Technologies, USA). Digital signals were transmitted over two custom 12-wire cables (CZ 1187, Cooner Wire, USA) that were counter-balanced with a custom system of pulleys and weights. Waveform extraction and automatic clustering were performed using Dataman (`https://github.com/wonkoderverstaendige/dataman`) and Klustakwik (Rossant et al., 2016), respectively. Clustered units were verified manually using the MClust toolbox.

During all experiments, video data was recorded using a CMOS video camera (Flea3 FL3-U3-13S2C-CS, Point Grey Research, Canada; 30 Hz frame rate) mounted above the arena. Animal position data was extracted offline using a convolutional deep neural network trained using transfer learning (Mathis et al., 2018).

Behavioral paradigms

We used three different behavioral paradigms: running on a linear track, open field exploration, and object exploration. In the linear track experiment (Figures 3A–D; Figure 5) mice were positioned at one end of track of a 1-meter long track with the task to run to the other end to collect a reward (a piece of Weetos chocolate cereal). After the animal consumed the reward, another reward was positioned on the opposite end. A lap was defined as an end-to-end run where the animal's body started from the first 10 cm of the track and reached the last 10 cm at the other end of the track without returning to its initial position. Recordings typically lasted between 20 and 30 minutes and experiments were performed on 10 consecutive days.

In the open field experiment (Figure 4), animals were free to explore an unfamiliar square arena (45 cm x 45 cm) for about 30 minutes. This was preceded and followed by a rest session in the animal's home cage ("Pre sleep" and "Post sleep") that typically lasted 60 minutes each.

The object exploration experiment (Figures 3F–J) was adapted from Deshmukh and Knierim (2011). Briefly, animals were free to explore a 75 cm x 75 cm square arena containing 3 objects for 5–7 consecutive trials (10 minutes each). Between trials, mice were returned to their home cages for 5 minutes. In each animal, the same procedure was performed on at least 3 consecutive days, resulting in 18 trials per animal that were included in the analysis. Object locations were kept constant for each animals throughout all trials.

Neural data analysis

For each identified spike unit, the signal-to-noise ratio (SNR) was used as a measure of electrophysiological signal quality (Figures 2A–E). The SNR was computed as the ratio between the peak absolute amplitude of the average spike waveform and noise on the tetrode channel on which the peak amplitude occurred (Meyer et al., 2018, Magland et al., 2020). To compute separate SNRs for "Active" and "Quiescent"

conditions for each unit (Figures 2D,E), recordings were first segmented using the 3-axis accelerometer signals from one of the recording headstages (sampled at 1000 Hz). Calibration of the accelerometer and extraction of head movement signals followed previous work (Meyer et al., 2018). Time points at which accelerometer-derived head movement signals exceeded 0.02 m/s^2 were assigned to the "Active" condition whereas all other time points were assigned to the "Quiescent" condition.

To assess the recording quality of the chronically implanted silicon probe across days, we analyzed the properties of sharp wave ripple (SWR) events (Figures 2G–K). LFP signals were down-sampled to 1 kHz and the analysis was restricted to periods when the animal was in the "Quiescent" state. First, data within these periods were filtered between 100-250 Hz using the "eegfilt" function (Delorme and Makeig, 2004). Then, for each animal, the channel with the highest amplitude was selected and defined as the pyramidal layer channel. All subsequent analysis steps were based on this channel. The envelope of the filtered signal was estimated in 10 ms windows, representing the ripple amplitude of each time series. Ripples were detected using a threshold (mean of the signal + 3 std) on the envelope. Additionally, the duration of the event had to exceed 40 ms. SWR duration was calculated using onset and offset of each event by identifying the points that crossed the mean of the signal + 1 std, before and after the detected peak in the envelope. SWR power was defined as the power at the peak of the envelope for each individual ripple event (Figure 2H). SWR duration was defined as the interval between the onset and the offset of each ripple event (Figure 2I). SWR frequency was calculated as the frequency at the peak value of the spectrogram computed for the SWR event (Figure 2J). The proportion of SWR was defined as the total number of SWRs divided by the duration of the quiescent state (Figure 2K). CA1 layers were estimated for each animal by combining the information provided by the depth profile of SWR complexes (Figure 2G), the theta power depth profile (Figure S4A), and the distance and displacement of the silicon probe contacts.

Generalized-Linear Model (GLM) with Poisson observations

We adopted a Poisson GLM to investigate how multiple behavioral variables and across-layer LFP signals from the silicon probe contribute to single-cell firing in the linear track experiment. The implementation of the GLM largely followed that of Hardcastle et al. (2017). Briefly, spike trains of single cells were binned at 100 ms. The animal's head position, head direction, and running speed were extracted from video data using a convolutional neural network (Mathis et al., 2018). Linear interpolation was used to temporally align the extracted behavioral data to the bin centers. For the position data, the linear track was divided into 25 non-overlapping bins (bin width 4 cm) along its major axis. For each time step, the indicator function (either 0 or 1) was used to indicate if a spatial bin is occupied by the animal. The same approach was used for head direction (24 bins of size 15°) and running velocity (12 bins of size 5 cm/s). As the firing of place cells can depend on the animal's running direction on a linear track, we used running velocity rather than running speed (where positive/negative velocity corresponds to the animal running to the far/near end of the track). In addition to the behavioral variables, theta (6–10 Hz) LFP amplitudes were extracted from either the electrode in the pyramidal layer (in which the tetrodes were positioned) or from all CA1 electrodes were included.

For each cell, a separate Poisson GLM was fit to the data using gradient descent on the negative log-likelihood (using the "minimize" function in the scipy Python package; Oliphant (2007)). Additionally, roughness penalties were introduced to enforce smoothness of the position, head direction, and running velocity GLM weights (Hardcastle et al., 2017); an L2 penalty was used for the theta amplitude weights. The hyperparameters determining the strength of the roughness and L2 penalties were found for each cell using grid search cross-validation ($N = 5$ folds). For each cell, the prediction accuracy of the different models ($\text{theta}_{\text{pyr}}$ and $\text{theta}_{\text{all}}$ in Figure 5E) was assessed using nested cross-validation ($N = 5$ folds). That is, the hyperparameters were determined using cross-validation on the training data and predictions were performed on the validation data. The data in Figure 5E were computed using the Poisson log-likelihood as described in (Hardcastle et al., 2017). Using the Pearson correlation between measured and predicted spike trains yielded qualitatively similar results.

Supplementary Figures

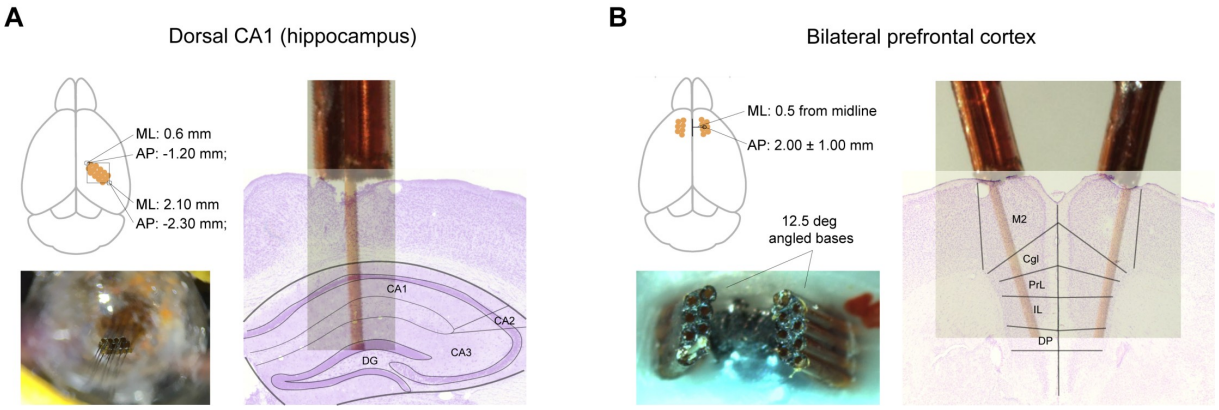

Figure S1: **The array design of the drive can be adapted to multiple areas and angles.** (A) Dorsal CA1 design. 5x3 tube array covering the dorsal CA1 area along its proximo-distal axis. Coordinates for the elliptic craniotomy are: top-left corner at AP: -1.20 mm; ML: 0.6 mm relative to bregma; bottom-right corner at AP: -2.30 mm; ML: 2.10 mm relative to bregma. The silicon probe (represented by the thicker tube in the image) is designed to cross all CA1 layers, while the tetrodes target the pyramidal layer. (B) Another example array design for bilateral prefrontal cortex recordings.

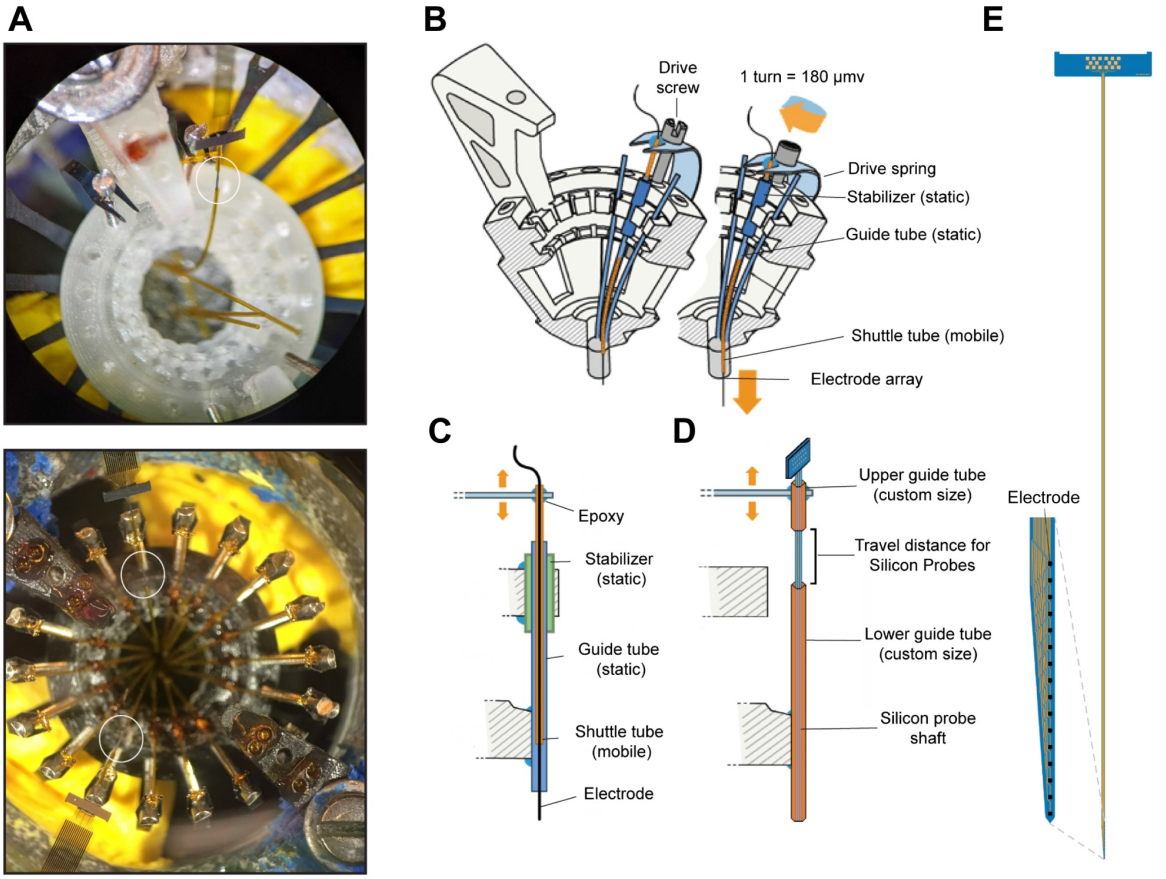

Figure S2: **Silicon probe and tetrode mechanism** (A) Picture illustrating the probe positioning and mechanism in the drive body. Upper image shows one silicon probe inserted in the guide tube. In the lower image two silicon probes are visible; the spring-screw mechanisms for tetrodes are assembled as well. The travel distance for the silicon probe is highlighted in the white circle. (B) Illustration of the spring-screw mechanism and the drive body, adapted from Voigts et al. (2013). (C) Detailed illustration of the spring-screw mechanism ensuring the independent movement of the tetrodes, adapted from Voigts et al. (2013). (D) Detailed illustration of the adapted spring-screw mechanism ensuring the independent movement of the silicon probes. (E) Illustration of the silicon probe currently in use for the CA1 design.

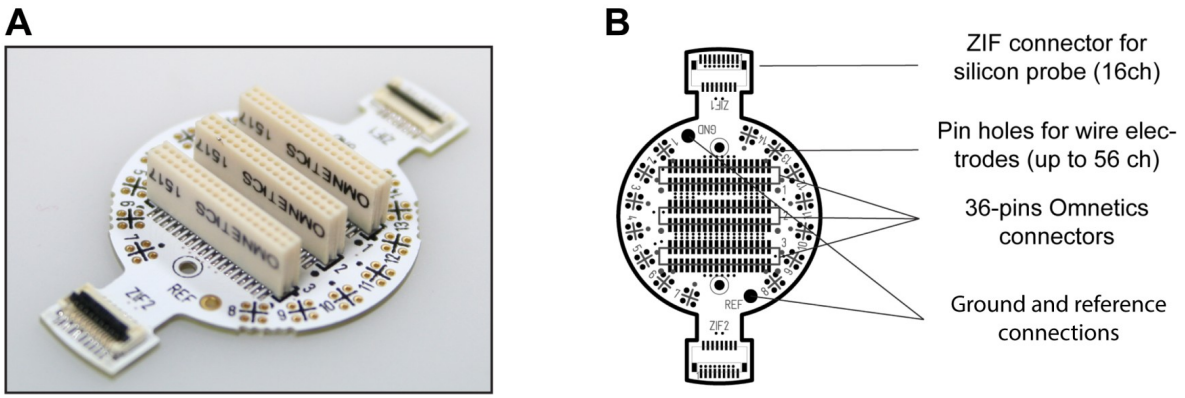

Figure S3: **EIB Design.** (A) EIB picture. (B) Illustration of the EIB design. The two lateral ZIF connectors for the silicon probes are integrated with the 36-pins Omnetics connectors in a compact design. 56 pin holes for wire electrodes allow to include up to 14 tetrodes. Ground and reference connections are positioned in between the ZIF and Omnetics connectors.

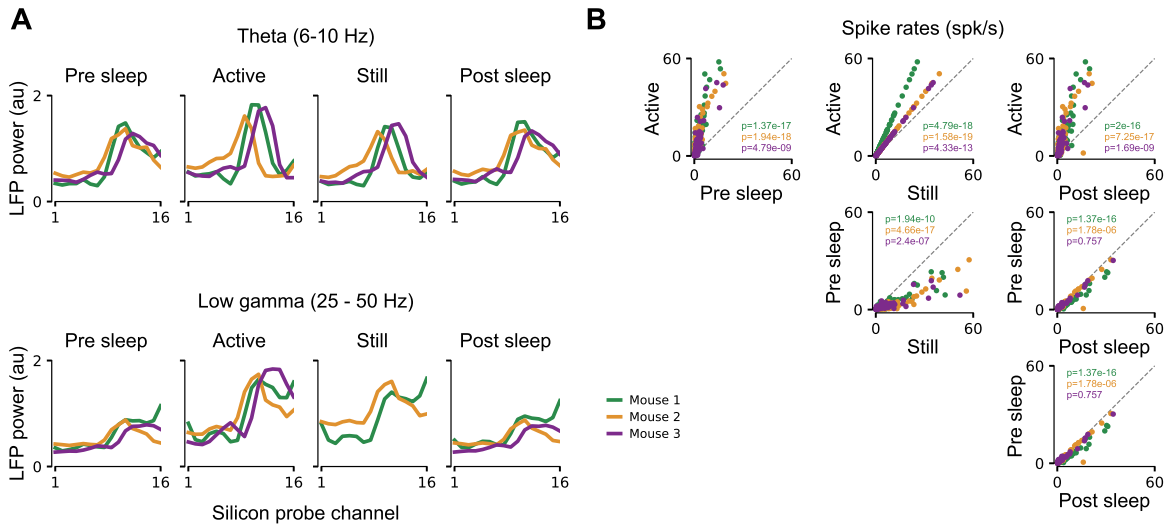

Figure S4: **Comparison of across-layer LFP power and spike rates for open field exploration and sleep. Related to Figure 4**. (A) LFP power for the different silicon probe electrodes spanning the vertical CA1 axis. Top: Theta band power for the different behavioral conditions in Figure 4. Bottom: The same but for the slow gamma frequency band. Colored lines indicate different animals. For each animal theta or slow gamma power in all conditions was normalized by the mean power in the active condition. (B) Average spike rates for single cells simultaneously recorded in the CA1 pyramidal layer. Same data and color scheme as in A. P-values were computed using a Wilcoxon rank-sum test (Bonferroni correction per animal).

Supplemental Movies

Movie S1: **Example mouse with a Hybrid Drive during different behavioral paradigms**.